International Forum on Aeroelasticity and Structural Dynamics
IFASD 2017
25-28 June 2017 Como, Italy

HIGH-FIDELITY CFD-CSM INTERACTION IN THE INDUSTRIAL CONTEXT

Bernd Stickan[1], Arne Rempke[2], Sebastian Helm[3], Hans Bleecke[4]

[1]Airbus Germany
Department of Aeroelasticity
Bernd.B.Stickan@airbus.com

[2]German Aerospace Center (DLR)
Institute of Aerodynamics and Flow Technology
Arne.Rempke@dlr.de

[3]University of Braunschweig
Institute of Aircraft Design and Lightweight Structures
Currently @ German Aerospace Center (DLR)
Institute of Aeroelasticity
Sebastian.Helm@dlr.de

[4]Airbus Germany
Department of Flight Physics Capability
Hans.Bleecke@airbus.com

Keywords: CFD-CSM, CFD mesh deformation, CFD mesh repair, nonlinear FEM, multi-body simulation, fluid-structure interaction

Abstract: The inclusion of structural deformations into aerodynamic computations is mandatory for nowadays highly accurate computational fluids dynamics (CFD) solvers. These CFD-CSM simulations are often performed with beam-stick structural models. This paper gives an overview about the usage of CFD-CSM interaction with very detailed structural models in an R+T context. Application examples are a detailed, but linear, AWIATOR test case FEM as well as multibody and nonlinear structural models for large civil aircrafts. For this kind of examples, the coupling method of aerodynamic and structural model has increased requirements. Additionally for complex aircraft configurations, the stability of CFD-CSM chains is reduced through the possibility of negative cell occurrances in the CFD mesh after deformation. A method using a finite-element method approach is introduced to repair these negative cells at runtime.

1 INTRODUCTION

Computational Fluid Dynamics (CFD) is used in a wide area of different industrial applications in aircraft development. While the focus is still on rigid applications, more and more interdisciplinary scenarios like static and dynamic fluid-structure interaction are on the rise.

The papers [1] and [2] give an impression about the accuracy which can be reached with high-fidelity CFD-CSM interaction for static and dynamic cases for a wind-tunnel model. The documents show for the examined clean-wing case the importance of high-fidelity aerodynamic

and structural modelling for transonic flow with shock-induced separation and cross-sectional deformations of the wing structure.

In the industrial context the same challenges appear. Hence, Section 3 handles the usage of very detailed structural models in static CFD-CSM computations.

In Section 2 the used methods and tools are briefly introduced.

2 METHODS AND TOOLS

2.1 CFD Solver:TAU

The DLR TAU-code is applied to solve the steady and the unsteady Reynolds Averaged Navier Stokes (RANS) equations [3]. The solver is working with a cell-vertex-based finite volume scheme on unstructured grids. In the following studies mainly the Spalart-Allmaras model [4] is used.

2.2 CSM Solvers

The applications presented in this paper use different structural solvers. These commercial solvers are:

- MSC-NASTRAN is the standard structural FEM solver in the context of aircraft aeroelasticity. In the context of this document only the linear static solution sequence is applied.
- MSC-ADAMS is a multi-body solver, which allows to combine multiple structural components from different regular structural models. The components itself are represented in generalized, modal format and, therefore, of linear type. But the interaction between the components due to body contacts and motion is handled nonlinearly. [5]
- DS-ABAQUS (DS=Dassault Systèmes) is used additionally due to its more powerful features concerning nonlinear structures. The main target of the here presented study is the handling of geometric nonlinearities. [6]

2.3 CFD-CSM Coupling

The coupling method for the aerodynamic and structural model uses a coupling matrix $\mathbf{G}_{\text{CFD,FEM}}$ which interpolates the structural displacements to the aerodynamic surface. The methodology allows to combine different interpolation methods for different model components. The selection of the interpolation method depends mainly on the available structural fidelity. The different coupling domains are united with blending and relaxation functions to keep a smooth and watertight CFD surface.

The general interpolation matrix $\mathbf{G}_{\text{CFD,FEM}}$ can be written as a product of the relaxation and blending matrices $\mathbf{M}_{Relax}$ and $\mathbf{M}_{Blend}$, which regulate the combination of different spline domains, and an interpolation method matrix $\mathbf{M}_{Splines}$:

$$\mathbf{G}_{\text{CFD,FEM}} = \mathbf{M}_{Relax} \cdot \mathbf{M}_{Blend} \cdot \mathbf{M}_{Splines}. \tag{1}$$

The matrix $\mathbf{M}_{Splines}$ contains the different interpolation method matrices:

$$\mathbf{M}_{Splines} = \begin{bmatrix} \mathbf{M}_{Spline\_1} & & & \\ & \mathbf{M}_{Spline\_2} & & \\ & & \ddots & \\ & & & \mathbf{M}_{Spline\_nSplines} \end{bmatrix}. \tag{2}$$

Each interpolation matrix $\mathbf{M}_{Spline\_i}$ may represent a different interpolation method.

The aerodynamic loads can be transferred to the structural surface using either the transposed interpolation matrix or a nearest-neighbour mapping.

More details about the methods can be found in [7].

2.4 CFD Mesh Deformation

The CFD mesh deformation is performed in two steps. The first step introduced in Section 2.4.1 is the deformation of all volume nodes with Radial Basis Function (RBF) interpolation plus an interpolation error correction method. The second step introduced in 2.4.2 is only triggered, if the first step produces very ill-shaped cells. If the volumes of such cells become negative, the mesh cannot be used by the CFD solver. In this case the mesh is fixed with a FEM approach mesh deformation method.

2.4.1 RBF Interpolation Plus Nearest Neighbour Correction

The algorithm is based on a group-weighting and a deformation blending approach of results of the Radial Basis Function (RBF) interpolation, see [8]. Afterwards, surface interpolation errors are fixed with a nearest neighbour correction.

Here the radial basis function interpolation approach is expanded with a linear interpolation polynomial $p(\boldsymbol{x}) = \beta_0 + \beta_1 x_x + \beta_2 x_y + \beta_3 x_z$.

$$s\left(\boldsymbol{x}\right) = \sum_{i=1}^{n} \alpha_i \phi\left(\|\boldsymbol{x} - \boldsymbol{x}_i\|\right) + p(\boldsymbol{x}). \tag{3}$$

This approach interpolates the scattered surface deformation input in points $\boldsymbol{x}_i$ to the volume mesh point $\boldsymbol{x}$, no cell connectivity is taken into account.

The group-weighting approach is used to allow the independent movement of different model parts/boundaries in the grid. Otherwise the deformations of different boundaries could influence each other and unintentional surface deformation would be the result. Separating the interpolation by each group protects the shape of the different bodies. Furthermore, since the number of RBF interpolation base points per group has a very large influence on the computational costs, this subdivision reduces the overall computational costs.

The deformation-blending approach supports the protection of boundary layer cells and the usage of radial basis functions $\phi(\|x\|)$ with limits $\phi(\|x\|) \to \infty$ for $\|x\| \to \infty$. These radial basis functions, which function value increases with increasing distance to the base point of a deforming body, need to be restricted further away from the surface of this body. Otherwise local deformations would influence the whole mesh. Additionally, the added polynomial of the interpolation approach (3) would deform the whole volume mesh as well. Consequently, the implemented approach to recover linear deformations exactly, cannot be used without blending of deformation values.

The computational costs are reduced through a strong reduction of the number of RBF interpolation base points. This means that the complete surface deformation information is not used in the RBF interpolation. Hence, the surface interpolation result is not accurate for points not used

as input. To overcome this inaccuracy, the volume points in a very close vicinity of the surface are corrected with the interpolation error of the closest surface point.

For more information on this mesh deformation method, it is referenced to [7] and [9].

2.4.2 Mesh Repair: FEM-based Mesh Deformation

As the mesh deformation described in the previous section is based on the set of nodes and does not know any volume elements within the mesh, it is unable to guarantee any properties of the volume elements of the deformed mesh. In fact there are some cases (see Section 3.2) which result in meshes with elements of (formal) negative volume. Such meshes cannot be used as a basis for finite-volume-based methods like the CFD-code TAU because they require proper elements with positive volume. In order to provide a deformed mesh without cells of negative volume, a more robust technique is applied to those parts of the mesh which need a repair.

The robust volume mesh deformation is implemented according to the elasticity analogy described in [10]. The mesh is modeled as an elastic solid with Lamé parameters E and ν of a virtual material. The Young's modulus E is variable and depends on the volume of the element e in the undeformed mesh:

$$E = \mathrm{vol}(e)^{-\chi},$$

where χ is a non-negative number controlling the intensity of stiffening smaller elements. With $\chi = 0.0$, the method reduces back to an elasticity model with constant material parameters. With $\chi = 1.0$, the method is identical to the proposal of [11]. In the general case of $\chi \neq 1.0$, the method allows different degrees of stiffening depending on the element size. The effect of stiffening smaller elements is an important feature for deforming CFD meshes with very anisotropic cells e.g. in the viscous boundary layer.

Instead of performing this deformation on the whole mesh, it is applied to the part of the mesh that needs to be repaired. As the crushed cells need to expand, it is necessary to relax the adjacent cells as well. However a too large area of repair makes the repair process unnecessary expensive in terms of computational costs. A good compromise is achieved by utilizing the following strategy proposed by [12]. After identifying the set of cells C_{negative} with a negative volume, all cells with at least one of the following properties are selected:

1. Cells within n_{repair} layers of cells surrounding those cells in C_{negative}, or
2. Cells within an Euclidean distance (measured in the deformed mesh) of fewer than a given positive distance d_{repair} from one of the cells in C_{negative}.

The union of the undeformed cells of these selections is used as the repair region Ω_{repair}. All boundaries of Ω_{repair} are equipped with the Dirichlet boundary condition and given displacement values provided by the RBF deformation method of the previous section. The partial differential equation of linear elastic behaviour is discretized with a linear finite-element-method on Ω_{repair}. The equation system is solved using the PETSc linear algebra routines [13].

The start parameters used are $\chi = 1.0$, $\nu = 0.3$, $n_{\mathrm{repair}} = 3$, $d_{\mathrm{repair}} = 0.0\mathrm{m}$. However, as the selected repair region might be too small or the virtual material parameters might not fit to the deformation task, some variations of these parameters are probed automatically until the resulting mesh does no longer contain any cells with negative volume.

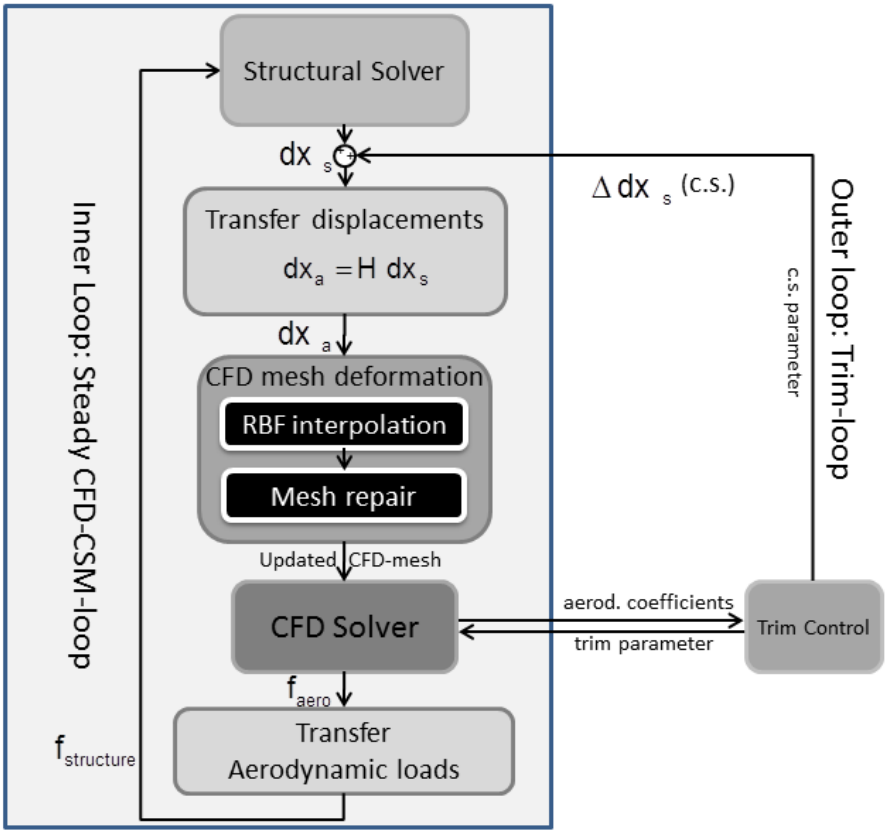

Figure 1: CFD-CSM loop sketch

2.5 Static CFD-CSM Interaction

The presented application examples of static CFD-CSM interaction are simply performed by iterating between the structural and the aerodynamic solver until convergence is reached.

An overview of the interaction chain can be seen in Figure 1. The simulation chain combines the structural and aerodynamic solver by using the coupling method sketched in Section 2.3. Since the coupling method involves only the model surfaces, the aerodynamic deflection must be transferred into the volumetric CFD mesh by mesh deformation introduced in 2.4. Notice here, that first the mesh deformation based on RBF interpolation is applied, and afterwards the mesh repair method is started to fix negative cells.

Additionally the model parameters can be used for trimming. For this purpose an outer iteration loop is implemented.

3 APPLICATION EXAMPLES

This section shows for several application examples the versatile field of static CFD-CSM interaction. The first two examples use AWIATOR flight test data. The data has already been used by Keye ([14]) for similar comparisons. These two examples use a classical linear structural model. Afterwards in Sections 3.3.1 and 3.3.2 a high fidelity multi-body model and a nonlinear wing-box FEM are used as structural model.

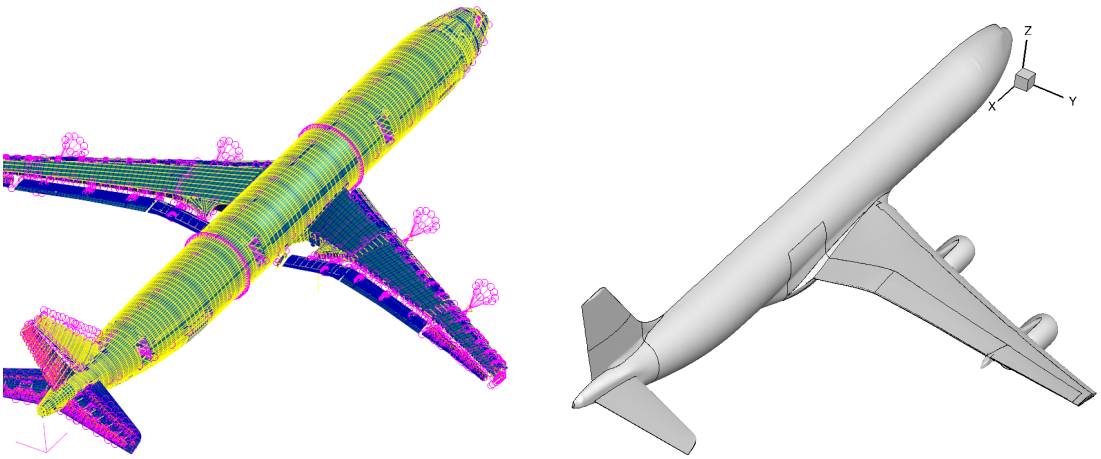

Figure 2: AWIATOR high speed: FEM and CFD model

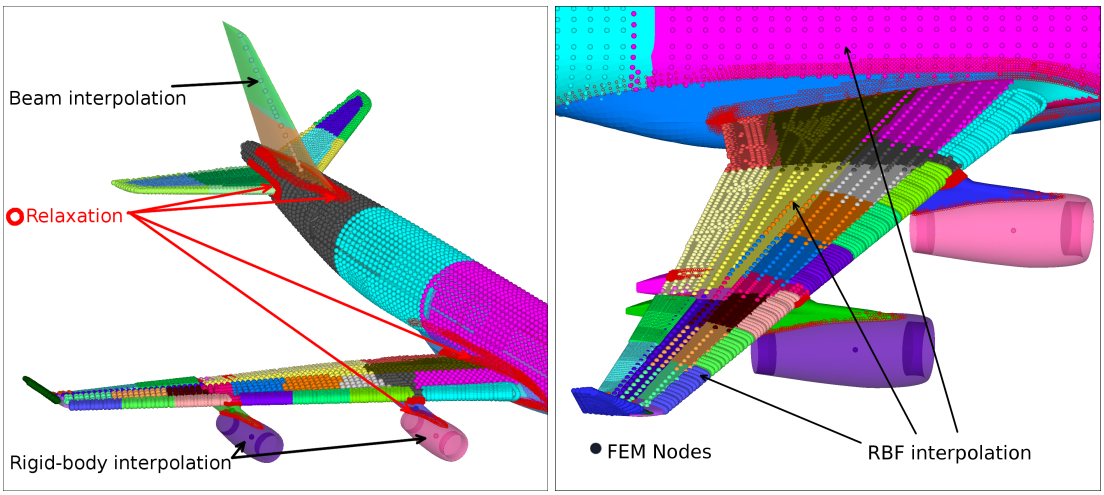

Figure 3: AWIATOR high speed: coupling setup

3.1 Linear Structure: AWIATOR High Speed

At first a high speed case at $Mach = 0.82$ and 41,000 feet altitude is presented. A longitudinal trim is performed for this flight point by varying the angle of attack and the HTP trim angle to match the lift C_{lift} and the pitching moment $C_{my} = 0.0$. As aerodynamic turbulence model the Spalart-Allmaras model has been used. The CFD mesh is a clean mesh without gaps at the control surfaces or similar features. The CFD model and the detailed FEM model including control surfaces is presented in Figure 2.

The first step towards the simulation results is the generation of the CFD-CSM coupling. Figure 3 shows this coupling setup. The different coupling groups of the setup are: Wing, horizontal tail plane (left and right), vertical tail plane (VTP), fuselage, inner and outer engine, inner and outer pylon. In the left plot the relaxation areas between the different groups are marked. Overall the two plots show a high number of different domains, identified with different colours. Most of the domains show a large number of scattered FEM nodes. For these domains RBF interpolation is used as surface interpolation method. The VTP and fairings are coupled with beam splines and the engines with rigid body splines. It can be observed that each control surface has its own coupling domain to perform component based interpolation and load transfer. An overlap of structural nodes shows a blending area between the interpolation domains.

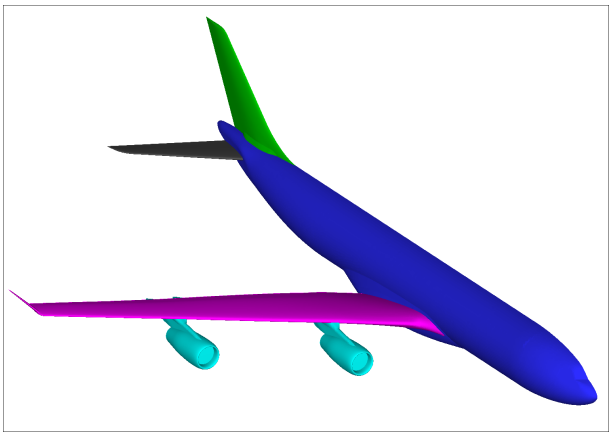

Figure 4: AWIATOR high speed: mesh deformation groups

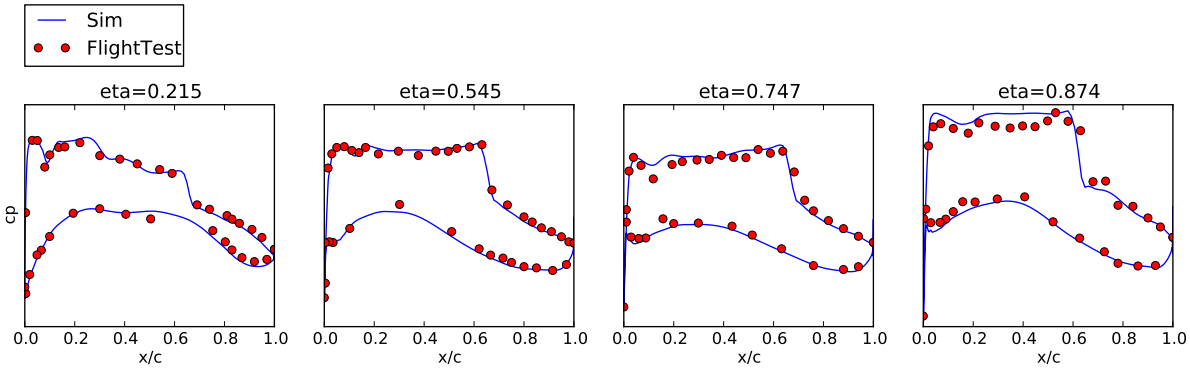

Figure 5: AWIATOR high speed: pressure comparison

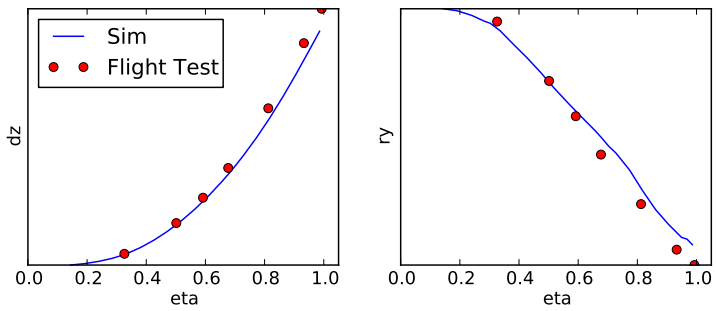

Figure 6: AWIATOR high speed: bend and twist comparison

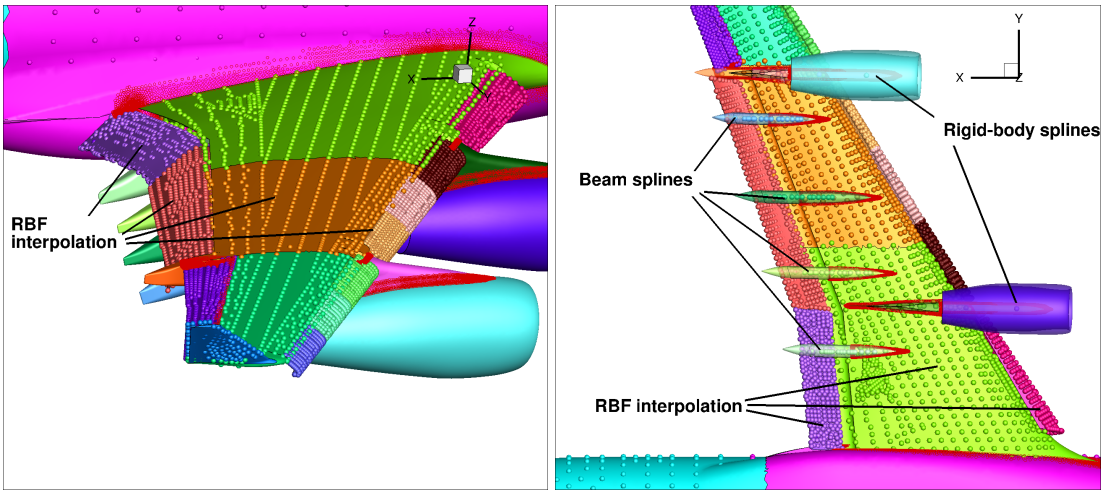

Figure 7: AWIATOR high lift case: coupling setup

The mesh deformation setup can be inspected in Figure 4. Each lifting surface and the fuselage are in different deformation groups. Additionally a deformation group for the engine, pylons and flap track fairings is used.

The comparison of pressures in Figure 5 and twist and bend in Figure 6 shows a good agreement between simulation results and flight test data. Shock positions are met accurately. The integrated local lift in the section at $eta = 0.874$ is slightly too high. The overprediction of the local incidence angle at the tip is also visible in the local twist in flow direction ry, which shows a larger nose-down effect in the flight test data close to the tip.

3.2 Linear Structure: AWIATOR High Lift

As second an AWIATOR test point at low speed is selected. The Mach-number is $Mach = 0.204$ at zero altitude. As for the previous case, a longitudinal trim is performed for the corresponding lift.

The structural model is the same as in the previous section, only the positions of control surfaces are changed. The CFD mesh is in this case different with respect to the previous section. It does in this case include all the gaps for the flaps and slats. Therefore, this test case is the best candidate to test the mesh repair feature presented in Section 2.4.2. The CFD mesh (half aircraft) has approx. 26 million nodes.

The coupling setup is shown in Figure 7 and the groups for the CFD mesh deformation in Figure 8. Figure 8 shows the undeformed and finally resulting deformed surface of the wing as well.

The selected settings of the RBF volume mesh deformation plus nearest-neighbour correction generate approx. 500 negative cells. The deformation state is very close to the final deformation state. The locations of these cells can be observed in Figure 9. The plot shows that negative cells are found on the complete wing, but mainly at the gap areas, e.g. at the gap between outer aileron and wing tip or wing-box and flap track fairings. The mesh repair method needs only three attempts to repair the mesh. Table 1 shows the evolution of settings and the number of negative cells. For a view on a slat-pylon intersection point the submesh of the mesh repair method is plotted in Figure 10 for each of the three attempts. It shows how the submesh Ω_{repair} is growing due to the increasing number of neighbour cells n_{repair}. It should be mentioned,

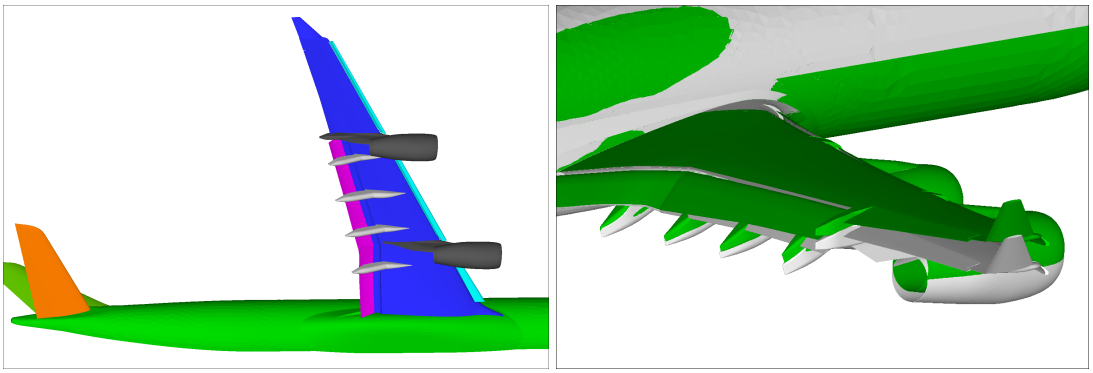

Figure 8: AWIATOR high lift case: left:rbf interpolation groups, right: undeformed (grey) and deformed (green) surface

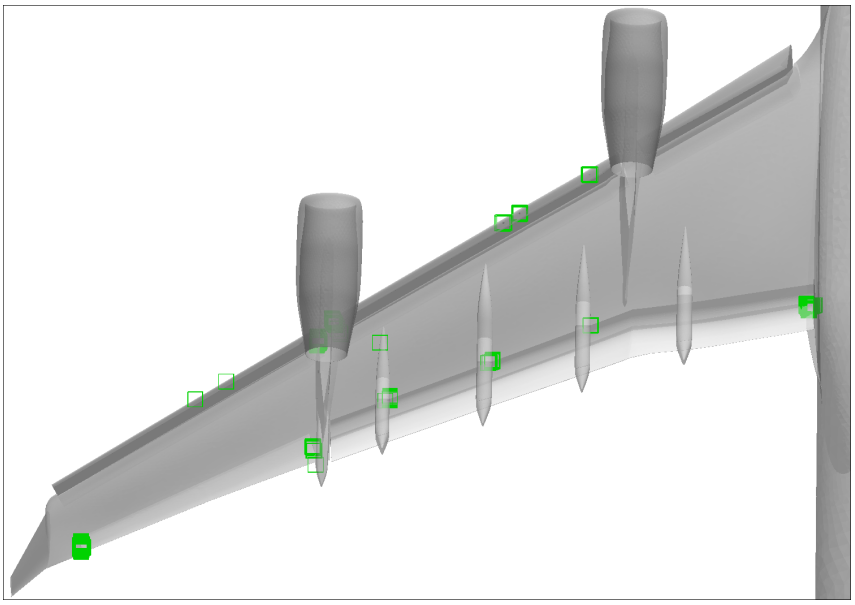

Figure 9: AWIATOR high lift case: locations of negative cells

that the computational costs of each try of the repair method have been smaller then the RBF deformation method.

attempt	χ	ν	n_{repair}	d_{repair}	$n_{\text{Nodes}}(\Omega_{\text{repair}})/10^3$	n_{NegCells}
1	1.0	3.0	3	0.0	108	5
2	1.0	3.0	5	0.0	179	10
3	1.0	3.0	10	0.0	410	0

Table 1: AWIATOR high lift case: Attempts to fix 500 negative cells

The resulting pressures can be compared to flight test in Figure 11. Again a good agreement can be found, but it should be kept in mind, that for such subsonic settings, the structural deflections do not have a very large influence on the pressure results.

Another case with the same simulation setup, but less adequate mesh deformation setting at the intersection area, could not be fixed by the mesh repair method. For this case 3100 negative cells have been produced by the mesh deformation method. The attempts with $n_{\text{NegCells}} > 200$ show a relatively high solution residual. However, at intermediate steps the repair method came quite close to fix the negative cells as shown in Table 2.

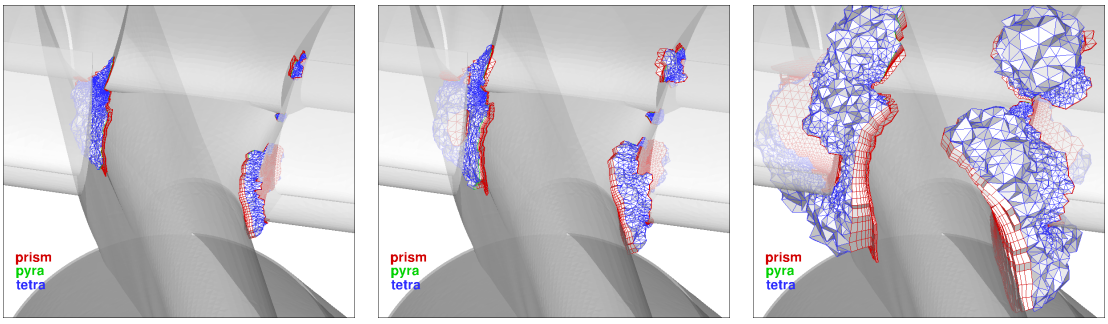

(a) Attempt 1: n_{repair}=3 (b) Attempt 2: n_{repair}=5 (c) Attempt 3: n_{repair}=10

Figure 10: AWIATOR high lift case: submeshes of mesh repair method

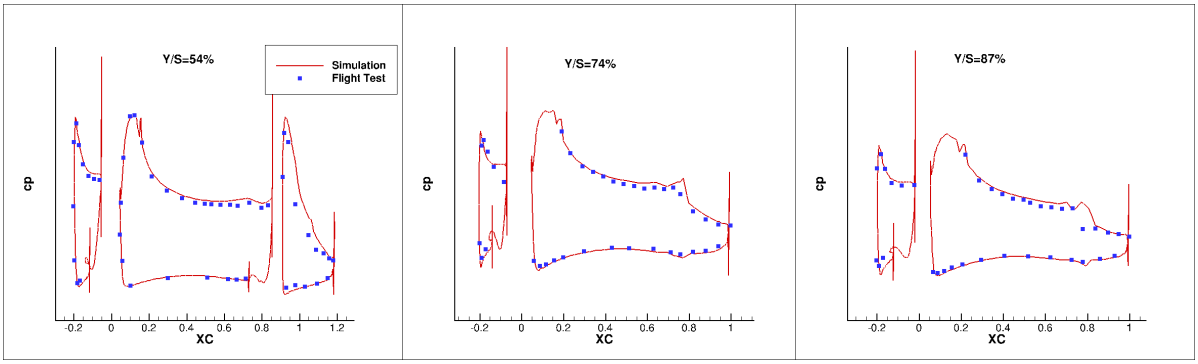

Figure 11: AWIATOR high lift case: pressure comparison

attempt	χ	ν	n_{repair}	d_{repair}	$n_{\text{Nodes}}(\Omega_{\text{repair}})/10^3$	n_{NegCells}
1	1.0	0.3	3	0.0	121	69
2	1.0	0.3	5	0.0	188	51
3	1.0	0.3	10	0.0	403	48
4	1.0	0.3	5	0.05	325	49
5	1.0	0.3	10	0.1	570	48
6	1.0	0.3	10	0.2	919	48
7	1.0	0.2	10	0.2	919	52
8	0.5	0.3	10	0.2	919	13
10	1.5	0.3	10	0.2	919	230
11	1.0	0.3	13	0.1	692	48
12	1.0	0.3	13	0.2	996	48
13	1.0	0.3	10	0.4	1882	48
14	1.0	0.3	15	0.2	1085	48
15	1.0	0.2	12	0.3	1375	52
16	0.5	0.3	12	0.3	1375	13
18	1.5	0.3	12	0.3	1375	234

Table 2: AWIATOR high lift case: Attempts to fix 3100 negative cells

3.3 Nonlinear Structural Models

This section contains two structural nonlinear examples. At first a multi-body simulation model with linear FEM components, but nonlinear component interaction (body/component kinematics as well as joints/contact kinematics including friction, backlash etc.) is used for a CFD-CSM application. Afterwards a nonlinear FEM taking into account geometric nonlinearities and dif-

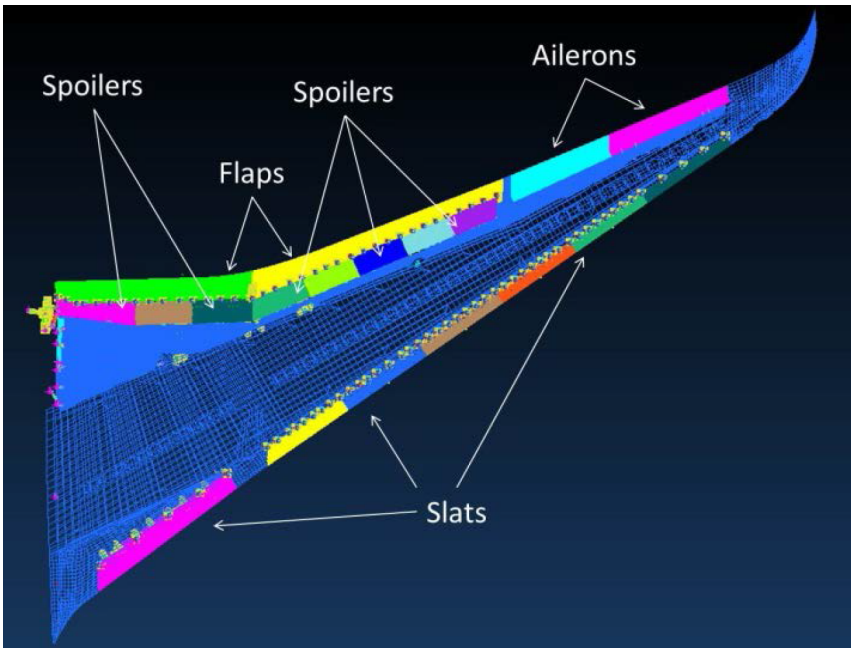

Figure 12: ADAMS wing MBS model

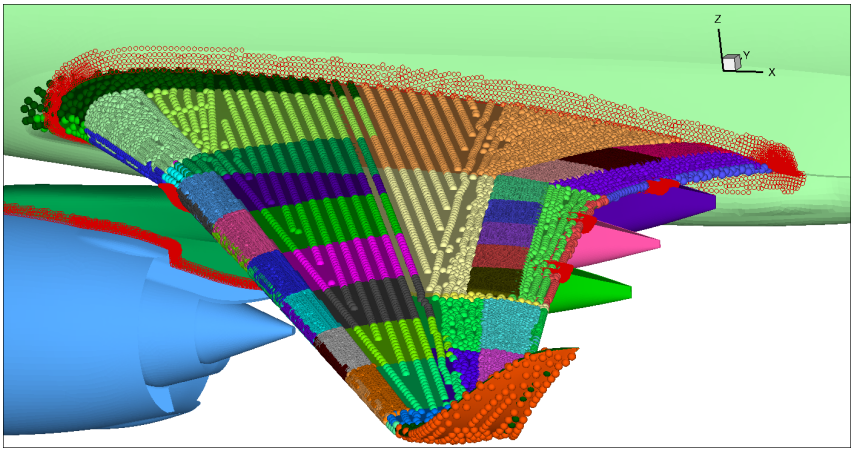

Figure 13: CFD-CSM coupling with MBS model

ferential stiffness is employed. Further results are going to be published in [15].

3.3.1 Structural Multi-Body Simulation Model

In this section a more complex structural model is used: a multi-body-simulation model consisting of several detailed FEM components. The coupling of FEMs and multi-body simulation is realized by the commertial software MSC ADAMS [5].

A top view of the model is visible in Figure 12. It shows all the approx. 20 components the model is based on: wing-box, 2 ailerons, 2 flaps, 7 slats and 7 spoilers.

The coupling to a clean CFD mesh can be seen in Figure 13. Here all the different components are visible, because the CFD and CSM part are bound together in many separated coupling domains.

A comparison of bending and twist to a regular linear FEM is available in Figure 14. It should be noted, that the clamping condition is not equal for both structural models. This might explain

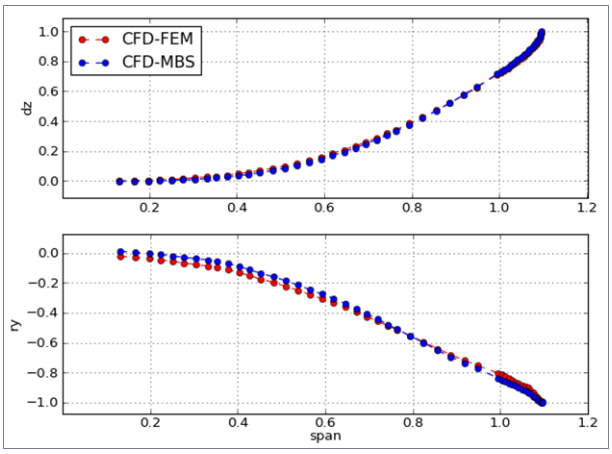

Figure 14: Bend-twist CFD-CSM result comparison of regular linear FEM and MBS model

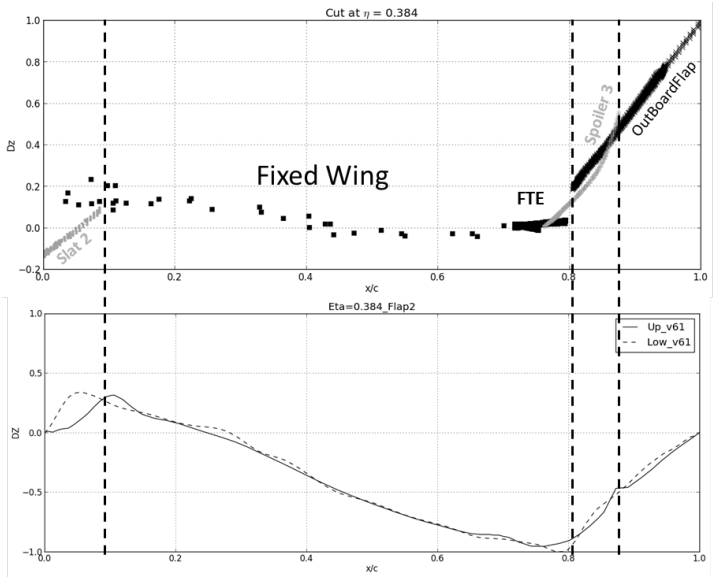

Figure 15: Cambering at wing cut; Top: Structural deformation; Bottom: CFD surface deformation

the visible differences in twist. But the agreement in bend is quite good.

In Figure 15 the chord-wise deformation is presented as relative displacements in z-direction (z), i.e. absolute bending and local angle of attack. It reflects the deformation of leading- and trailing edge movables and the transition between the wing and movable surfaces in detail. The largest deflections are observed at the trailing edge. This upward deflection of trailing edge devices, essentially a de-cambering, is observed over the whole wing span. Another observation is the occurrence of steps at the transition between fixed wing and movable surfaces. As can be seen in the bottom part of Figure 15, the deformation is globally well transferred to the CFD surface. The CFD model and the mesh deformation are, however, limiting the precise transfer of sharp edges due to mesh quality constraints. Therefore, the blending introduced by the coupling method leads to a smearing of steps.

Concerning the stability of such a simulation setup, it should be expected that so many components, moving with respect to each other, further increase the problem of negative cells.

More information on the usage of this MBS model can be found in [16]. On specific CFD-CSM simulations with this setup it is referred to [17].

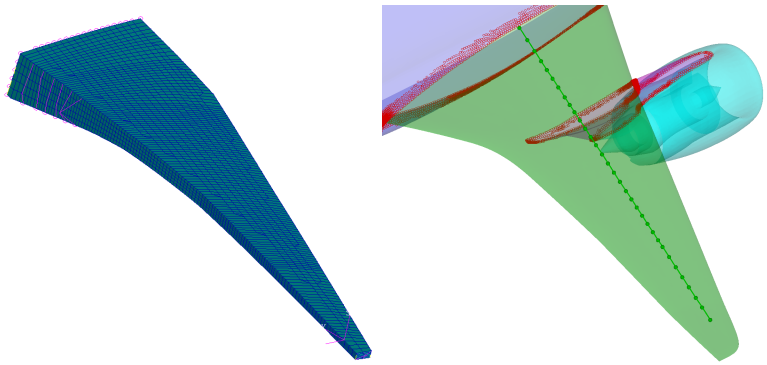

Figure 16: Nonlinear wing-box FEM and corresponding beam coupling to CFD model

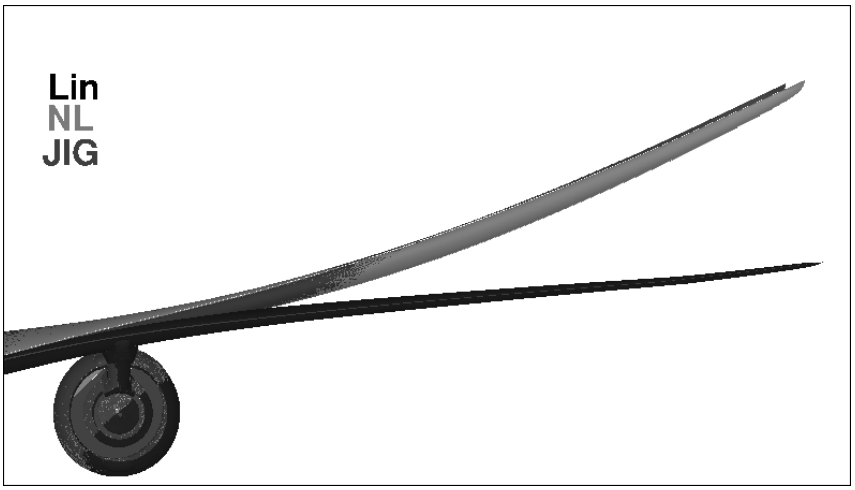

Figure 17: Nonlinear CSM: Comparison of deformed CFD surface for linear (lin) and nonlinear (NL) FEM at constant $C_{\text{lift}} = 0.85$, additionally the JIG shape is plotted

3.3.2 Nonlinear Structure

As application example for nonlinear deformations a transport aircraft CFD model is coupled with an ABAQUS structural model of a relatively flexible wing-box. The flow conditions are subsonic at $Mach = 0.5$.

Here the results of 3 investigated C_{lift} values are presented. To get an impression of the overall deformation, the deformed CFD surface for the highest C_{lift} is plotted in Figure 17. The large amount of deformation is clearly visible.

ABAQUS allows to compute the model in linear and nonlinear sense. In Figure 18 the bend and twist (local angle of attack) of linear and nonlinear FEM is compared at constant C_{lift}. The structural deflections at the tip are up to 16 percent of the span, which reflects again the flexibility of the model. Furthermore it can be observed that the linear FEM exhibits a prolongation of the wing compared to the nonlinear case.

Table 3 compares the relative wing prolongations $\Delta\text{span}_{\text{rel}} = (\text{span}_{\text{JIG}} - \text{span}_{\text{Defo}}) \,/\, \text{span}_{\text{JIG}}$ and drag differences $\Delta C_{\text{drag,rel}} = (C_{\text{drag,NL}} - C_{\text{drag,Lin}}) \,/ C_{\text{drag,Lin}}$ for the different C_{lift} cases. The linear FEM model span increases up to 1.6 percent for the highest CL in the deformed state while the nonlinear FEM case shows negligible span increase. This difference is reflected in the drag as well. The drag for the nonlinear computation decreases by up to 1 percent.

The results show that for a very flexible wing the selection of appropriate structural models is

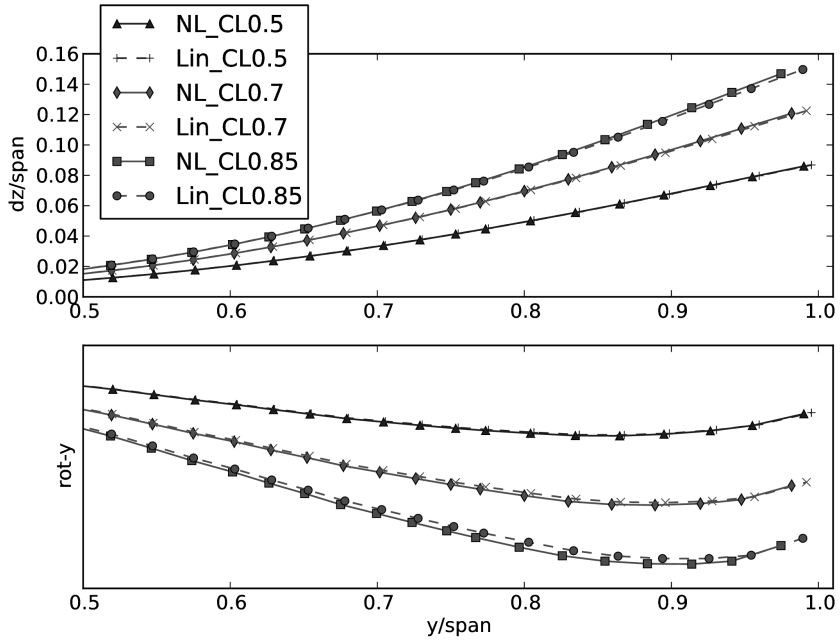

Figure 18: Nonlinear CSM: Comparison of bend and local angle of attack (rot-y) for linear (lin) and nonlinear (NL) FEM at constant C_{lift}

C_{lift}	$\Delta\mathrm{span}_{\mathrm{rel,lin}}$ [%]	$\Delta\mathrm{span}_{\mathrm{rel,NL}}$ [%]	$\Delta C_{\mathrm{drag,rel}}$ [%]
0.50	0.552	0.0058	-0.059
0.70	1.100	0.0077	-0.268
0.85	1.641	0.0081	-1.094

Table 3: Nonlinear CSM: Comparison of relative wing prolongation and relative drag-difference for linear (lin) and nonlinear (NL) FEM at constant C_{lift}

essential for accurate CFD-CSM results. And it should be underlined that for more relevant transonic Mach-numbers the differences are very likely to be more significant.

4 CONCLUSION

The studies in this paper have shown the variety of applications for CFD-CSM interaction. Not only linear structural models have been employed, but also multi-body simulation and nonlinear structural models have been used for certain applications. The robustness of such simulations is not only endangered by convergence issues of the involved disciplines aerodynamics and structure (for nonlinear models). The main point of failure is the deformation of complex CFD meshes. Here a method based on FEM based mesh deformation is used to repair negative cells in the CFD mesh. The method of FEM-based mesh deformation turned out to be very powerful to overcome this robustness issue. Since only first, but promising, mesh repair studies have been shown, further experience must be collected with this new method in the future.

5 REFERENCES

[1] Stickan, B., Dillinger, J., and Schewe, G. (2014). Computational aeroelastic investigation of a transonic limit-cycle-oscillation experiment at a transport aircraft wing model. *Journal of Fluids and Structures*, 49(0), 223 – 241. ISSN 0889-9746.

[2] Stickan, B., Dillinger, J., and Nitzsche, J. (2015). Limit-cylcle-oscillation simulations of aerostabil windtunnel experiments 2. In *International Forum on Aeroelasticity and Structural Dynamics (IFASD), St. Petersburg*.

[3] Gerhold, T. and Galle, M. (1997). Calculation of complex three-dimensional configurations employing the DLR TAU-code. *AIAA Paper 97-0167*.

[4] Spalart, P. and Allmaras, S. R. (1992). A one-equation turbulence model for aerodynamic flows. AIAA Paper 92-0439.

[5] MSC. *MSC-ADAMS*. URL:www.mscsoftware.com.

[6] Systémes, D. *DS-ABAQUS*. URL:www.3ds.com.

[7] Stickan, B., Bleecke, H., and Schulze, S. (2013). Nastran based static cfd-csm coupling in flowsimulator. In N. Kroll, R. Radespiel, J. W. Burg, and K. Srensen (Eds.), *Computational Flight Testing*, vol. 123 of *Notes on Numerical Fluid Mechanics and Multidisciplinary Design*. Springer Berlin Heidelberg. ISBN 978-3-642-38876-7, pp. 223–234.

[8] Heinrich, R., Kroll, N., Neumann, J., et al. (2008). Fluid-Structure Coupling for Aerodynamic Analysis and Design - A DLR Perspective. *46th AIAA Aerospace Sciences Meeting and Exhibit 2008, Reno*.

[9] Barnewitz, H. and Stickan, B. (2013). Improved mesh deformation. In B. Eisfeld, H. Barnewitz, W. Fritz, and F. Thiele (Eds.), *Management and Minimisation of Uncertainties and Errors in Numerical Aerodynamics*, vol. 122 of *Notes on Numerical Fluid Mechanics and Multidisciplinary Design*. Springer Berlin Heidelberg. ISBN 978-3-642-36184-5, pp. 219–243.

[10] Stein, T. T., K. and Benney, R. (2003). Mesh moving techniques for fluid-structure interactions with large displacements. *Journal of Applied Mechanics*, 70, 58–63.

[11] Tezduyar, B. M. M. S., T. E. and Johnson, A. A. (1992). Computation of unsteady incompressible flows with the finite element methods – space- time formulations, iterative strategies and massively parallel implementations. *New Methods in Transient Analysis, P. Smolinski, W. K. Liu, G. Hulbert, and K. Tamma, eds.*, 143, 7–24.

[12] Rempke, A. (2016). Netzdeformation mit elastizitatsanalogie in multidisziplinärer flowsimulator-umgebung. In *20th STAB DGLR Conference,Brunswick, Germany*.

[13] Balay, S., Abhyankar, S., Adams, M. F., et al. *PETSc Web page*. URL=http://www.mcs.anl.gov/petsc, Accessed: 04-20-2017.

[14] Keye, S. (2011). Fluid-Structure Coupled Analysis of a Transport Aircraft and Flight-Test Validation. *Journal of Aircraft*, 48(2), 381–390.

[15] Stickan, B., Schröder, F., Helm, S., et al. (2017?). On recent advances in industrial high-fidelity aeroelasticity. In R. Heinrich (Ed.), *AeroStruct Enable and Learn how to Integrate Flexibility in Design*, Notes on Numerical Fluid Mechanics and Multidisciplinary Design. Springer Berlin Heidelberg.

[16] Landwehr, U. (2015). Multi-body simulation - simulation of flight control surfaces functioning. *Mobiles - Fachzeitschrift für Konstrukteure*, 38, 36–39.

[17] Helm, S., Haupt, M., B.Stickan, et al. (2015). Advancements of cfd-csm coupling by means of multibody simulation. In *Deutscher Luft- und Raumfahrtkongress Rostock, 22-24.9.2015*.

COPYRIGHT STATEMENT